Volume 4
Number 10
October 2025
Pages 817–918

Sensors & Diagnostics

rsc.li/sensors

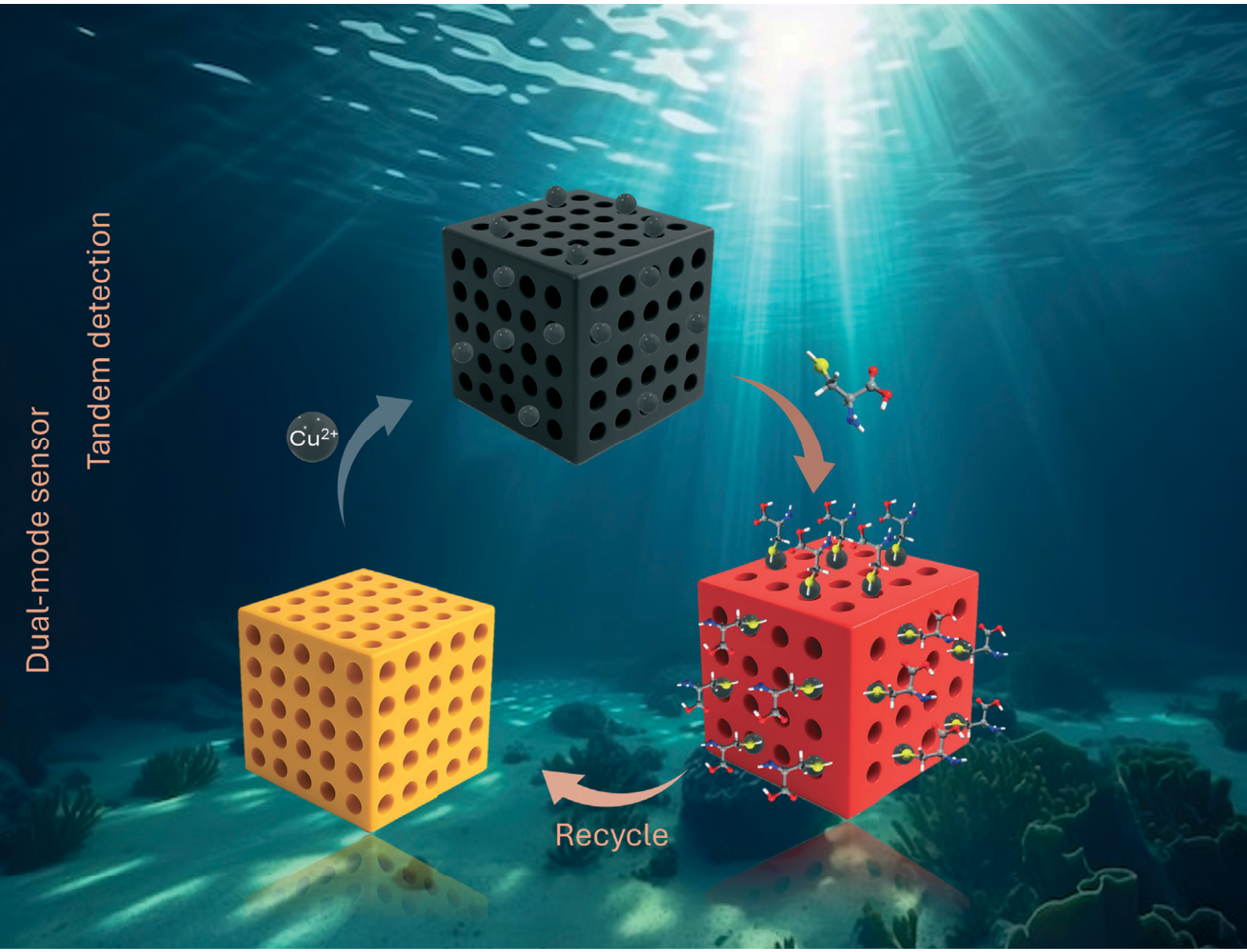

ISSN 2635-0998

ROYAL SOCIETY OF CHEMISTRY

PAPER
Venkata Suresh Mothika *et al.*
Reversible dual-mode detection of Cu^{2+} and tandem capture of cysteine using a salphen-conjugated microporous polymer

Sensors & Diagnostics

PAPER

View Article Online
View Journal | View Issue

Cite this: *Sens. Diagn.*, 2025, **4**, 846

Reversible dual-mode detection of Cu^{2+} and tandem capture of cysteine using a salphen-conjugated microporous polymer

Nilojyoti Sahoo,† Atul Kapoor,† Monika Yadav, Saurabh Kumar Rajput and Venkata Suresh Mothika *

Conjugated microporous polymers (CMPs) possess extended π-conjugation combined with microporosity, enabling amplified sensing response even with ultra-trace solution or vapor-phase analytes, and their high sensing response output was demonstrated with several CMPs. However, CMPs exhibiting tandem detection properties, *i.e.*, sequential detection of multiple analytes, are rarely reported and represent the next generation of CMP chemical sensors offering enhanced sensitivity and specificity. Herein, we report the design and synthesis of a salphen-conjugated microporous polymer (pTPE-salphen) for reversible dual-mode (fluorometric/colorimetric) nanomolar detection of Cu^{2+} ions and tandem capture of cysteine (Cys). pTPE-salphen synthesized *via* Schiff-base condensation between 1,1,2,2-tetrakis(4-hydroxy-3-formylphenyl)ethene and *o*-phenylenediamine, emits yellow photoluminescence (PL) at λ_{Em}^{max} = 537 nm with a PL quantum yield of 5.41%. pTPE-salphen exhibited remarkable thermal stability up to 425 °C and a fused spherical nanoparticle morphology. pTPE-salphen showed strong PL quenching up to 92% when exposed to Cu^{2+} (50 μM), selectively among other metal ions, due to the ground-state complex formation of Cu^{2+}@pTPE-salphen. pTPE-salphen was highly sensitive to Cu^{2+} with a detection limit of 5.69 nM and exhibited a high Stern–Volmer constant (K_{SV}) value of 8.12×10^6 M^{-1}. Notably, the pTPE-salphen-based paper strip sensor showed appreciable sensitivity up to 10^{-11} M Cu^{2+}. In addition, strong colorimetric changes from yellow (R/B is 1.9) to black (R/B is 0.53) were also observed upon the formation of Cu^{2+}@pTPE-salphen, and the binding of Cu^{2+} was confirmed by XPS analysis. Interestingly, Cu^{2+}@pTPE-salphen exposed to cysteine (Cys) exhibited reversible colorimetric response from black to orange (R/B is 1.8) both in dispersion and paper strip sensors due to the formation of Cys–Cu^{2+}@pTPE-salphen where Cys binds with Cu^{2+} anchored on the pore surface of pTPE-salphen, and the entire colorimetric process (yellow ⇌ black ⇌ red) is reversible. The binding of Cys to Cu^{2+} and its tandem capture were systematically studied using XPS and NMR. Such sequential detection and capture (tandem process) of Cu^{2+} and Cys using a conjugated microporous polymer sensor is unique and of high significance in environmental and biological applications.

Received 18th June 2025,
Accepted 1st August 2025

DOI: 10.1039/d5sd00097a

rsc.li/sensors

1. Introduction

Sequential detection of metal ions and biomolecules *via* dual-response sensing mechanisms such as reciprocal fluorometric/colorimetric or electrochemical modes, also referred to as tandem detection, offers a robust and reliable detection method with enhanced sensitivity and specificity.[1] Such tandem detection holds great promise for the development of next-generation chemical sensors for environmental monitoring, biological analysis, and diagnostic applications.[2] However, achieving tandem detection requires a carefully designed sensor capable of facilitating specific coordination interactions between metal ions and biomolecules. The copper ion (Cu^{2+}), a redox-active transition metal ion, and cysteine (Cys), a thiol-containing amino acid, exhibit such a relationship.[3,4] Their strong and selective binding interactions enable not only effective tandem detection but also, in some cases, capture or removal of Cu^{2+} by cysteine.[5]

Cu^{2+} is essential for physiological homeostasis, mitochondrial respiration, oxidative stress regulation, neurotransmitter production, *etc.*[6] The World Health Organization (WHO) recommends Cu^{2+} levels below 2 ppm in drinking water and 10–22 μM in serum.[7] Hypocupric states can lead to anemia, immunosuppression, and neurodevelopmental defects, while excess Cu^{2+} is associated

Department of Chemistry, Indian Institute of Technology (IIT), Kalyanpur, Kanpur, 208016, India. E-mail: smothika@iitk.ac.in
† NS and AK contributed equally.

with hepatotoxicity, oxidative damage, and neurodegenerative diseases like Alzheimer's, Parkinson's, *etc.*[8,9] Cys, meanwhile, is crucial for cellular redox homeostasis, protein folding through disulfide bond formation, metal detoxification, and glutathione biosynthesis.[10] Fluctuations in Cys levels are associated with cardiovascular diseases, liver dysfunction, immune deficiencies, and neurological disorders.[11]

Compared to conventional analytical techniques such as atomic absorption spectroscopy (AAS), inductively coupled plasma mass spectrometry (ICP-MS), and high-performance liquid chromatography (HPLC), optical sensor-based detection of metal ions offers easy signal readout, low cost, portability, and suitability for onsite applications.[12–15] Several fluorescent sensors were developed based on different recognition units such as Schiff bases, coumarin, and triazole derivatives for Cu^{2+} detection, demonstrating their performance in aqueous media and real sample analysis.[16–18] The optical detection has been further extended to low-cost paper strip sensors, a facile and instrument-free sensing platform for rapid naked-eye analysis on-site.[19,20] Similarly, quantification of subtle colorimetric changes of sensors upon exposure to metal ions was traceable *via* smartphone-assisted RGB analysis, providing a user-friendly and digital detection system.[21]

Recently, tandem detection of Cu^{2+} has gained significant attention as it provides enhanced selectivity and sensitivity compared to single-mode optical sensors.[22] Ahmed *et al.* reported reversible tandem detection of Cu^{2+} and Cys or L-histidine using an *o*-hydroxy hydrazone-based covalent organic framework (COF) as a fluorescence on–off–on sensor.[23] Ding *et al.* reported a hydrazide hydrazone-based small molecule sensor as a fluorescence on–off–on sensor for the simultaneous detection of Cu^{2+} and homocysteine.[8] You *et al.* reported sequential detection of Cu^{2+} and Cys based on the hydrazide hydrazone-based colorimetric sensor.[24] Tandem detection of other metal ions was also reported in the literature. Yan *et al.* and Park *et al.* reported a turn-on sensor based on a water-soluble cyclodextrin fluorescent probe and Au nanoclusters for tandem detection of Hg^{2+} and Cys, respectively.[25,26] Shen *et al.* reported tandem detection of Al^{3+} and norfloxacin based on fluorescent Au-doped Cu-nanoclusters.[27] Yang *et al.* reported tandem detection of H_2S and Cu^{2+} using a UiO-66-MA metal–organic framework (MOF) as a fluorescence off–on–off sensor.[28]

Recently, conjugated microporous polymers (CMPs) have emerged as a unique class of porous organic polymers (POPs) for chemical sensing applications.[29–31] They exhibit excellent optical signal transduction properties due to extended conjugation, leading to efficient exciton migration, and exhibit amplified signal response even in the presence of ultra-trace analytes.[32,33] CMPs offer flexibility to prepare smooth thin films of controllable thickness/roughness suitable for sensing device applications.[34] Single-mode CMP chemical sensors have been reported for the detection of metal ions, biomolecules, explosives, *etc.*[35] However, CMPs exhibiting dual-mode response and tandem detection properties, particularly for Cu^{2+} and Cys, were rarely reported yet are unique and require careful choice of building blocks. Herein, we report a salphen-bridged fluorescent tetraphenylethene (TPE) based CMP (pTPE-salphen) exhibiting both fluorometric and colorimetric responses (dual-mode) upon binding with Cu^{2+}, wherein the complexation of Cu^{2+} with salphen units forming Cu^{2+}@pTPE-salphen was responsible for the visible color change (yellow to black) and fluorescence quenching response. Interestingly, Cu^{2+}@pTPE-salphen showed a strong visible color change (black to orange) when exposed to Cys due to the selective binding of Cys to the Cu^{2+} present on the pore surface of pTPE-salphen. A paper strip-based pTPE-salphen sensor further showed reversible colorimetric changes when sequentially exposed to Cu^{2+} and Cys, illustrating its tandem detection properties. Due to the high density of salphen units and high surface area, pTPE-salphen resulted in excellent sensitivity to Cu^{2+} and exhibited very low detection limits of 5.69 nM with a high Stern–Volmer constant (K_{SV}) value of 8.12×10^6 M^{-1}.

2. Experimental section

2.1 Materials and instrumentation

o-Phenylene diamine, 4,4′-dihydroxybenzophenone, titanium tetrachloride ($TiCl_4$), boron tribromide (BBr_3), and hexamethylenetetramine (HMTA) were procured from Spectrochem. *n*-Butanol, *o*-dichlorobenzene (*o*-DCB), and dry triethylamine (Et_3N) were purchased from Spectrochem, while Zn dust and hydrochloric acid (HCl) were acquired from Rankem. All amino acids were obtained from SRL Chemicals. All the above chemicals, reagents, and solvents are analytically pure and used without further purification. Anhydrous solvents such as *N*,*N*′-dimethylformamide (DMF) and tetrahydrofuran (THF) were freshly distilled under a nitrogen atmosphere according to standard procedures. The stock solution of metal salts was prepared in distilled water with chloride salts of Fe^{2+}, Hg^{2+}, Co^{2+}, Mg^{2+}, Ca^{2+}, Zn^{2+}, Mn^{2+}, Cd^{2+}, Ni^{2+}, and Cu^{2+}, and all the dilutions were performed with distilled water. ^{1}H NMR spectra (solution-state) were recorded using a JEOL ECX 400 MHz spectrometer with deuterated chloroform ($CDCl_3$) and dimethylsulfoxide (DMSO-d_6) as the solvent and tetramethyl silane (TMS) as an external standard. The solid-state ^{13}C-CP/MAS NMR spectrum was measured on a Bruker Avance NEO 400 MHz spectrometer and interpreted using MestReNova software. FTIR spectra were recorded in the range of 500–4000 cm^{-1} using a Perkin Elmer 1000 UATR instrument in ATR mode. Thermogravimetric analysis (TGA) was carried out under a N_2 atmosphere on a Mettler Toledo TGA/DSC 1 Star System from 25 to 800 °C at a heating rate of 10 °C min^{-1}. Powder X-ray diffraction (PXRD) measurements were collected using a PANalytical X'Pert diffractometer. Morphological analysis was conducted using scanning electron microscopy (SEM, FEI NOVA NANO SEM 450) by drop-casting ethanol-dispersed samples onto Al foil.

Transmission electron microscopy (TEM) images were acquired on an FEI Tecnai G2 12 Twin 120 kV instrument by drop-casting ethanolic dispersions onto a carbon-coated copper grid. N_2 adsorption–desorption isotherms were recorded at 77 K using an AUTOSORB-iQ analyzer after degassing samples at 120 °C for 12 h. Photoluminescence spectra were recorded on a Fluoromax-4 spectrometer from Horiba Scientific. The time-correlated single photon counting (TCSPC) measurements have been carried out using a home-built custom setup with a 405 nm picosecond-pulsed diode laser (DeltaFlex, HORIBA Scientific). Solid-state diffuse reflectance UV-vis spectra were collected using a JASCO V-770 spectrophotometer. Solution-state UV-vis absorption spectra were measured with a JASCO UV-vis–NIR double-beam spectrometer. X-ray photoelectron spectroscopy (XPS) was performed using a Thermo Scientific NEXSA surface analysis system equipped with a monochromatic Al Kα radiation source ($h\nu$ = 1486.69 eV). All graphical data representations, including fluorescence, adsorption studies, spectroscopy, electrochemical analyses, and TGA plots, were prepared using OriginPro 2022 software. Electrochemical measurements, including cyclic voltammetry (CV) and electrochemical impedance spectroscopy (EIS) analysis, were conducted using a PalmSens PS4.F2.05 electrochemical workstation in a standard three-electrode setup comprising a 3 mm glassy carbon (GC) working electrode, a Ag/AgCl (0.1 M KCl) reference electrode, and a platinum wire as the counter electrode. For electrode modification, CMP polymer dispersion (1 mg mL^{-1} in CH_2Cl_2) was drop-casted onto a pre-polished GC electrode and air-dried at room temperature. The monomer M1 was synthesized by adopting the procedures reported previously.[36–38]

2.2 Synthesis of the pTPE-salphen CMP

In a J Youngs Schlenk tube, M1 (200 mg, 0.393 mmol, 1 eq.) and *o*-phenylenediamine (84 mg, 0.786 mmol, 2 eq.) were dissolved in 6 mL of a 1 : 1 (v/v) mixture of *n*-butanol and *o*-dichlorobenzene and aq. CH_3COOH (6 M, 0.5 mL). The reaction mixture was sonicated for 10 minutes and subjected to three freeze-pump-thaw cycles and heated at 120 °C for 4 days. The solids formed are filtered, washed with acetone, methanol, and further purified using Soxhlet extraction with CH_2Cl_2 for 24 hours. The resulting yellow solids were dried and used for further analysis. Yield: 75%.

2.3 Fluorescence quenching experiments

For calculating the fluorescence quenching efficiency (QE), 50 μM of aq. Cu^{2+} solution was added to pTPE-salphen dispersion in DMF (0.5 mg mL^{-1}), and the fluorescence intensities were measured before and after addition. The %QE was calculated using the following eqn (1),

$$\%QE = [1 - F/F_0] \times 100 \quad (1)$$

where F_0 and F represent the fluorescence intensity of the pTPE-salphen CMP before and after the addition of Cu^{2+}, respectively.

The selectivity experiments were performed similarly by adding different aqueous solutions of metal ions (50 μM), and the corresponding %QE values were determined and compared with those of Cu^{2+}. For fluorescence titration experiments, aliquots of aq. Cu^{2+} (0–100 μM) were added gradually to the DMF dispersion of pTPE-salphen (0.5 mg mL^{-1}) and the fluorescence was measured continuously. For nanomolar concentration studies, individual solutions containing pTPE-salphen and Cu^{2+} were prepared, and the fluorescence collected was plotted as F_0/F *vs.* $[Cu^{2+}]$ to obtain the Stern–Volmer plots and limit of detection values. 390 nm excitation was used in all the fluorescence experiments.

2.4 Preparation of the paper strip sensor

The filter paper was cut into 1 × 1 cm square pieces and dipped in pTPE-salphen CMP dispersion (0.5 mg mL^{-1}) and dried under air at room temperature. To these paper strips, a solution of aq. Cu^{2+} ions of different concentrations (10^{-4}–10^{-11} M) was sprayed, and the changes in their fluorescence were captured before and after contact with the Cu^{2+} solution. In the colorimetric sensing, the paper strips were prepared similarly, and the changes in their visible color under daylight were captured when exposed to Cu^{2+} (50 μM) and cysteine solutions (0.5 mM).

3. Results and discussion

3.1 Synthesis and characterization

The pTPE-salphen CMP was synthesized in a J Young Schlenk tube *via* the Schiff base condensation reaction between 1,1,2,2-tetrakis(4-hydroxy-3-formylphenyl)ethene (M1) and

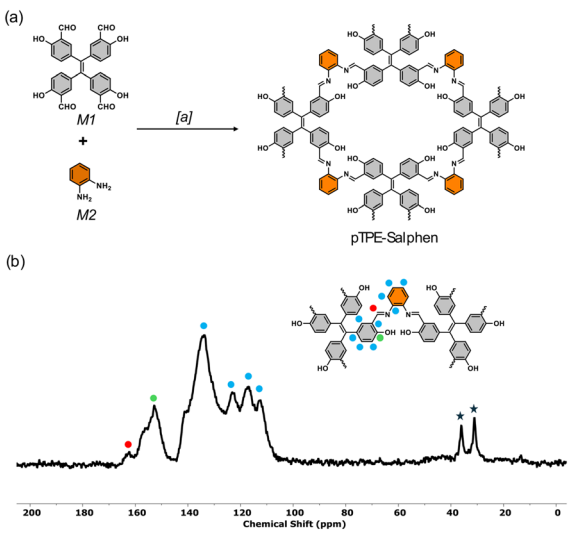

Fig. 1 (a) Synthetic route of the preparation of pTPE-salphen. [a] *n*-BuOH/*o*-DCB/AcOH (1 : 1 : 0.2), 120 °C, 96 h. (b) Solid state ^{13}C-CP MAS NMR spectrum of pTPE-salphen. Peaks with a star indicate spinning side bands.

o-phenylenediamine (M2). The monomer mixture was suspended in a 1 : 1 mixture of *n*-BuOH, *o*-DCB, and 6 M AcOH catalyst (Fig. 1a) and subjected to degassing by three freeze-pump-thaw cycles and then heated at 120 °C for 4 days. The obtained light-yellow solids were isolated by filtration and purified by Soxhlet extraction, yielding the pTPE-salphen CMP as a light-yellow solid (see Experimental section). The Fourier transform infrared spectra (FTIR) of pTPE-salphen exhibited stretching vibrations at 1670 cm^{-1} ($\nu_{C=N}$), confirming the formation of imine (C=N) linkages and a broad band between 2950 and 3575 cm^{-1} (ν_{O-H}) corresponding to hydrogen-bonded OH. The free OH at *ca.* 3626 cm^{-1} present in M1 disappeared in the CMP, suggesting a possible involvement of phenolic OH in the H-bonding with the imine of the pTPE-salphen CMP (Fig. S1). The stretching frequencies of the NH (ν_{N-H}) of *o*-phenylenediamine and the carbonyl ($\nu_{C=O}$) of M1 disappeared in the pTPE-salphen CMP, indicating successful imine condensation, and the absence of any monomeric impurities in the CMP. The solid-state ^{13}C cross polarization magic angle spinning (CP MAS) nuclear magnetic resonance (NMR) spectrum of the pTPE-salphen CMP displayed characteristic carbon peaks of the imine and phenolic unit at 162 and 152–156 ppm, respectively, suggesting the successful formation of the salphen unit *via* Schiff base condensation (Fig. 1b). Other peaks in the range of 110–140 ppm are assigned to other aromatic carbons. The chemical environment of the elements present in pTPE-salphen was analysed using X-ray photoelectron spectroscopy (XPS). The deconvoluted C1s spectrum showed three peaks at 284.60, 285.64, and 286.56 eV corresponding to the carbon of 'C=C', 'C=N' of the imine, and 'C–O' of the phenolic unit, respectively (Fig. 2a). On the other hand, the deconvoluted N 1s spectrum in Fig. 2b revealed two peaks at 398.8 and 400.6 eV corresponding to the nitrogen of 'C=N' and 'C–N' which are consistent with the reported salphen-based porous organic polymers (POPs).[23,39] Similarly, deconvolution of the O 1s spectrum (Fig. 2c) revealed two peaks centered at 531.9 and 533.1 eV corresponding to the oxygen of phenolic OH and 'C–O' functionalities, respectively. This further confirms the presence of imine linkages within the network leading to the formation of the salphen-cored CMP. The powder X-ray diffraction pattern of pTPE-salphen showed a broad peak in the range of 5–50° and indicated its amorphous nature (Fig. 2d). The pTPE-salphen CMP was found to show exceptional thermal stability, as evidenced by the thermogravimetric analysis (TGA), and the pTPE-salphen did not show any weight loss up to 425 °C; however, upon further heating, *ca.* 28% weight loss was observed until 800 °C (Fig. 2e). N_2 adsorption/desorption isotherms of activated pTPE-salphen measured at 77 K up to a relative pressure (P/P_0) of 1 atm exhibited a type-II adsorption profile with a total gas uptake of 150 mL, and the Brunauer–Emmett–Teller (BET) surface area was calculated to be 29.7 $m^2\ g^{-1}$ (Fig. S2). Field emission scanning electron microscopy (FESEM) analysis of pTPE-salphen revealed fused spherical-like nanoparticles of sizes 0.5 to 1 μm (Fig. 2f). Similar fused spherical particles were observed by high-resolution transmission electron microscopy (HRTEM), and at high magnifications the presence of several stacks of CMP sheets was observed (Fig. 2f and S3). Further, elemental mapping (EDS)

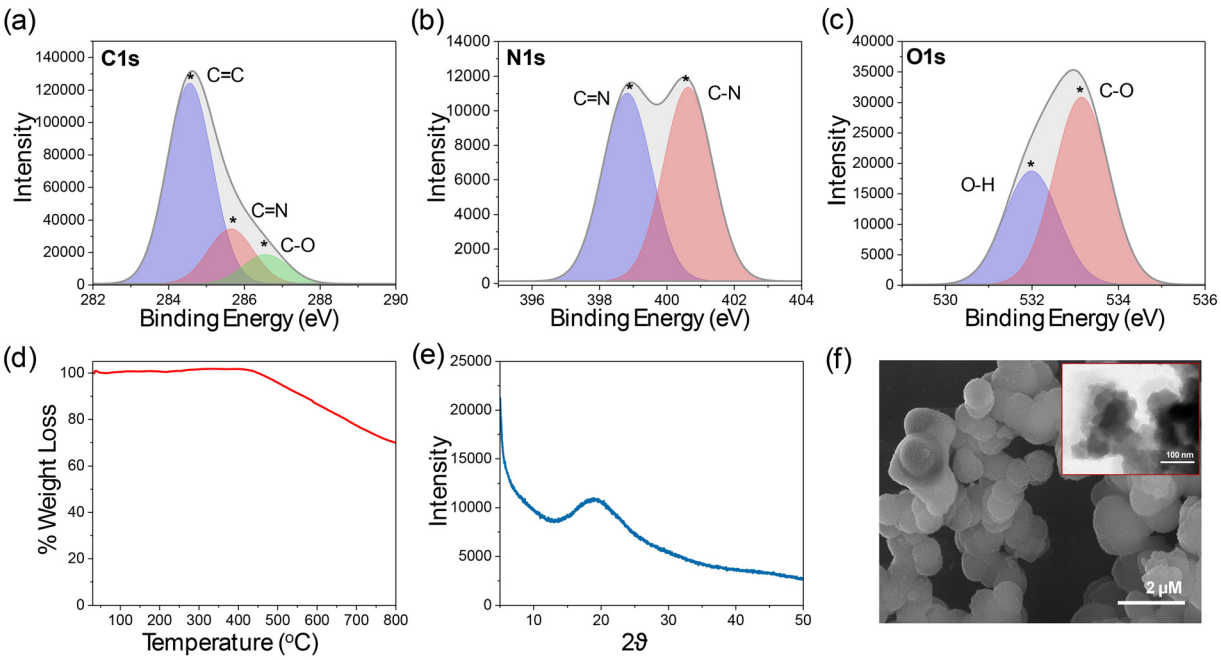

Fig. 2 (a–c) Deconvoluted C 1s, N 1s, and O 1s XPS spectra of pTPE-salphen, (d) TGA plot, (e) PXRD, and (f) SEM image of pTPE-salphen. High magnification TEM image is shown in the inset.

indicated the distribution of elements C, N, and O throughout the polymer network (Fig. S4 and S5).

3.2 Fluorescence of pTPE-salphen and selective sensing of Cu^{2+}

pTPE-salphen consists of an aggregation-induced emission (AIE) active TPE unit conjugated to a salphen core, and the intramolecular H-bonding between phenolic OH and imine can result in excited-state intramolecular proton transfer (ESIPT) emission due to keto–enol tautomerism. As shown in Fig. S6, the fluorescence emission maximum of pTPE-salphen bathochromically shifted by increasing the solvent polarity. In a non-polar solvent like toluene, pTPE-salphen showed fluorescence with emission maximum at 425 nm associated with the high-energy enol form.

On the other hand, in a highly polar aprotic solvent like DMF and DMSO, pTPE-salphen exhibited emission majorly at *ca.* 537 nm associated with the radiative decay from the keto form. Interestingly, the emission intensity was significantly enhanced in polar solvents like DMF, due to the restricted rotation of TPE phenyl in polar solvents and improved conjugation with salphen units along the polymer chains. Such restricted rotation-induced emission enhancement was also observed in TPE-based porous polymers reported earlier. The relative fluorescence quantum yield of pTPE-salphen was determined to be 5.41% in DMF. Based on these results, DMF was chosen as the solvent medium for fluorescence sensing studies. All the analytes were taken in their aqueous solution. Initially, the PL response of pTPE-salphen was measured by adding 50 μM of Cu^{2+} to pTPE-salphen dispersion in DMF. As shown in Fig. 3a, nearly 92% of PL quenching was observed selectively with Cu^{2+} and only a mere quenching was observed with other metal ions such as Co^{2+}, Ni^{2+}, Mg^{2+}, Cd^{2+}, *etc.* Moreover, the relative fluorescence quantum yield was found to decrease to 0.44% upon the addition of 50 μM of Cu^{2+}, indicating a significant quenching effect of Cu^{2+} on the CMP. PL titration experiments by gradual addition of Cu^{2+} (0–100 μM) resulted in gradual PL quenching of pTPE-salphen (Fig. 3b). The fitting of the F_0/F *vs.* [Cu^{2+}] plot resulted in a non-linear relationship between PL quenching and Cu^{2+} concentration (Fig. 3c). The PL quenching was also evident from the images of pTPE-salphen before and after the addition of Cu^{2+} captured under UV-light (Fig. 3a inset). However, the fluorescence quenching performed at the nanomolar concentration resulted in a linear relationship between F_0/F and [Cu^{2+}] and the fitting to the equation $F_0/F = (1 + K_{SV}[Cu^{2+}])$ resulted in a Stern–Volmer constant (K_{SV}) value of 8.12×10^6 M^{-1} (Fig. 3d), where F_0 and F are the fluorescence intensities of the CMP before and after the addition of Cu^{2+}. To further understand the fluorescence quenching pathway, excited state lifetime analysis of pTPE-salphen was performed by gradual addition of Cu^{2+} (0–50 μM). As seen in the τ_0/τ *vs.* [Cu^{2+}] plot (Fig. 3c inset and S7), the excited state lifetime of pTPE-salphen gradually decreased upon the addition of Cu^{2+}. The above results suggest that at lower concentration (nM range), the complexation of Cu^{2+} to the salphen unit of the CMP is mainly responsible for the fluorescence quenching (static quenching); however, at higher concentration, fluorescence quenching was possibly due to a combination of static and dynamic quenching pathways where the interchain excited state energy transfer between TPE conjugated salphen units and Cu^{2+} bound salphen present within the polymer network contribute to the dynamic quenching. The limit of detection (LoD) calculated from the F_0/F *vs.* [Cu^{2+}] plot (nM range) by employing the equation LoD = $3\sigma/K$, where σ represents the standard deviation, was found to be 5.69 nM. Interestingly, pTPE-salphen exhibited high selectivity for Cu^{2+} when compared to other metal ions studied. As shown in Fig. S8 and S9, pTPE-salphen showed relatively low fluorescence quenching efficiency when added with 50 μM of other metal ions like Co^{2+}, Ni^{2+}, Cd^{2+}, Mg^{2+}, Fe^{2+}, Hg^{2+}, Ca^{2+}, Zn^{2+}, Mn^{2+}, *etc.* The above results indicated that pTPE-salphen is a highly selective Cu^{2+} sensor and exhibits remarkably ultralow detection limits. To determine the association constant (K_a) values, Benesi–Hildebrand plots were deduced from fluorescence titration experiments.

The Benesi–Hildebrand equation can be represented as eqn (2),

$$1/(F_0 - F_i) = \{1/[K_a(F_0 - F_{min})]\}[Cu^{2+}] + 1/(F_0 - F_{min}) \quad (2)$$

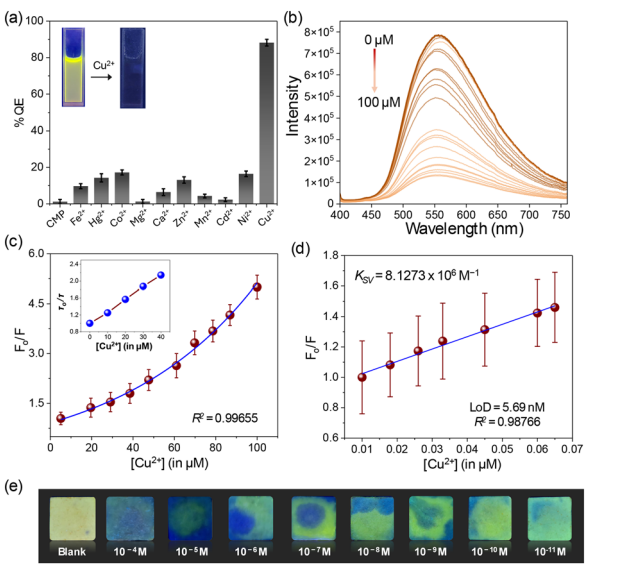

Fig. 3 pTPE-salphen fluorescence quenching analysis: (a) quenching efficiency of Cu^{2+} compared with other metal ions (inset: images of pTPE-salphen before and after Cu^{2+} addition), (b) gradual fluorescence quenching of pTPE-salphen upon the addition of Cu^{2+} (0–100 μM) and (c) corresponding F_0/F *vs.* [Cu^{2+}] showing non-linear relationship. Inset: changes in excited state lifetime with the addition of Cu^{2+} (0–50 μM). (d) Linear fitting of the Stern–Volmer plot F_0/F *vs.* [Cu^{2+}] in the nanomolar Cu^{2+} concentration range. (e) pTPE-salphen coated paper test strips under UV light showing appearance of non-fluorescent dark spots upon exposure to Cu^{2+} (10^{-4} to 10^{-11} M).

Here, F_0 and F_i represent the fluorescence intensity of pTPE-salphen before and after the addition of varying concentrations of Cu^{2+}, and F_{min} corresponds to the fluorescence intensity in the presence of an excess amount of Cu^{2+}. The association constant (K_a) of the Cu^{2+}@pTPE-salphen determined from $1/(F_0 - F_i)$ *vs.* $1/[Cu^{2+}]$ was found to be 1.53×10^5 M^{-1} (K_a = intercept/slope) (Fig. S10). Such high K_a values indicate strong binding interactions between pTPE-salphen and Cu^{2+}.

3.3 Contact mode detection of Cu^{2+}

Contact-mode analysis using the paper-strip-based sensor further suggested the efficacy of pTPE-salphen in trace-level sensing of Cu^{2+}. The paper test strips coated with the pTPE-salphen CMP were exposed to Cu^{2+} ions (10^{-4} to 10^{-11} M), and the corresponding fluorescence changes were captured by UV light irradiation. As seen in Fig. 3e, the paper strips exposed to Cu^{2+} (up to 10^{-9} M) resulted in significant non-fluorescent spots at the contact regions. This PL quenching is ascribed to the complexation of Cu^{2+} to the salphen unit of pTPE-salphen and formation of non-fluorescent Cu^{2+}@pTPE-salphen. The PL response of the paper strip pTPE-salphen sensor indeed highlighted its suitability for practical detection of ultra-low Cu^{2+} present in water resources of real-world environmental conditions. Remarkably, fluorescence response was also observed at ultra-low Cu^{2+} concentrations (10^{-9}–10^{-11} M). These results corroborate well with the PL measurements in the dispersion state with the addition of the nM concentration of Cu^{2+} to the pTPE-salphen.

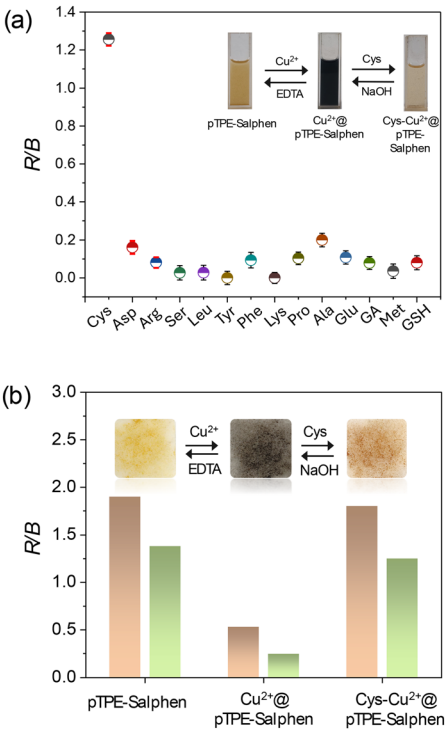

Fig. 4 Smartphone RGB analysis: (a) selective colorimetric response of Cu^{2+}@pTPE-salphen to cysteine among other amino acids and corresponding R/B ratios in DMF dispersion. The corresponding daylight images are shown in the inset. (b) Bar graph for paper-based test strips (orange) & solution mode (green) showing changes in R/B ratios of pTPE-salphen, Cu^{2+}@pTPE-salphen, and Cys–Cu^{2+}@pTPE-salphen with corresponding daylight color changes in the inset.

3.4 Tandem detection of cysteine

Cu–salen complexes, known to bind cysteine selectively, were adopted for porous organic polymers for tandem detection applications, either by fluorometric or colorimetric methods. For instance, Ahmed *et al.* reported turn-on tandem detection of cysteine using a Cu^{2+}-loaded hydrazone-hydrazide COF, wherein the emission of the COF regenerated upon exposure to cysteine due to the formation of a Cu–Cys complex.[23] Unlike the COF, the Cu^{2+} bound pTPE-salphen CMP (represented as Cu^{2+}@pTPE-salphen) upon the addition of cysteine did not result in regeneration of CMP's emission, but resulted in a strong colorimetric change (black to orange). Unlike small molecular salen complexes, the salphen-integrated CMP studied here is insoluble in organic solvents and does not allow the study of the interactions between Cu^{2+}@pTPE-salphen and cysteine by solution-state UV/vis spectroscopy. In order to overcome this limitation, a smartphone-assisted, instrument-free RGB analysis technique was used to illustrate the cysteine detection properties of Cu^{2+}@pTPE-salphen. Such an RGB technique was reported previously and offers a simple, rapid, and cost-effective approach to study the target analytes onsite, and also circumvent the challenges of identifying visual color changes by the naked eye.[40] The RGB approach of colorimetric detection of analytes was previously adopted for Pb^{2+}, glutathione, and norflaxcin detection using polymers.[41–44] When 0.5 mM Cys was added to a dispersion of Cu^{2+}@pTPE-salphen (0.5 mg mL^{-1}), the color of the dispersion changed from dark to light orange-yellow, and the color changes were captured by a smartphone camera (OnePlus Nord CE4, 50 MP Sony OIS Camera) positioned at a constant distance of 25 cm. The RGB values from the recorded images were analysed using the Color Analyzer App to represent the colorimetric response. As shown in Fig. 4a, the R/B ratio of Cu^{2+}@pTPE-salphen significantly changed upon the addition of Cys, suggesting a strong interaction between cysteine and Cu^{2+}@pTPE-salphen, potentially due to the coordination of cysteine to the Cu^{2+} of Cu^{2+}@pTPE-salphen. Interestingly, the response was found to be selective for cysteine and no considerable colorimetric changes (R/B ratio) were observed when Cu^{2+}@pTPE-salphen was exposed to other amino acids such as asparagine (Asp), arginine (Arg), serine (Ser), leucine (Leu), tyrosine (Tyr), phenylalanine (Phe), lysine (Lys), proline (Pro), alanine (Ala), glutamic acid (GA), methionine (Met) and glutathione (GSH) (Fig. S11). Such selective binding of Cys to Cu^{2+}–salen complexes or polymers was reported in the literature and explored for tandem detection of Cys.[7,23,24,45] Such tandem cysteine detection by Cu^{2+}@pTPE-salphen also demonstrates the high specificity

of pTPE-salphen toward Cu^{2+} within a complex matrix of competing metal ions, mimicking real-world environmental conditions.

3.5 Insights into cysteine binding and capture

Systematic FTIR analysis was carried out at different stages to investigate cysteine binding to the Cu^{2+}@pTPE-salphen. As shown in Fig. S12, upon coordination of Cu^{2+} with the salphen unit of pTPE-salphen, the imine stretching frequency ($\nu_{C=N}$) band shifted from 1670 to 1650 cm^{-1}, and the free OH stretching vibration (ν_{O-H}) at 3625 cm^{-1} disappeared. This confirms the binding of Cu^{2+} to the salphen unit and formation of Cu^{2+}@pTPE-salphen. Upon cysteine capture, the IR spectrum of Cys–Cu^{2+}@pTPE-salphen showed complete disappearance of characteristic bands of free SH (ν_{S-H} = 2560 cm^{-1}) and NH (ν_{N-H} = 3300–3500 cm^{-1}) stretching frequencies of cysteine, indicating the binding of cysteine to Cu^{2+} *via* chelation. XPS analysis was performed to further understand the coordination changes occurring during the sequential incorporation of Cu^{2+} and cysteine within the pTPE-salphen CMP. As shown in Fig. 5a and S13, Cu^{2+}@pTPE-salphen exhibited two peaks at 933.52 eV (Cu $2p_{3/2}$) and 953.33 eV (Cu $2p_{1/2}$), confirming successful metallation of the salphen core. Further, the N 1s XPS spectrum (Fig. 5b and S13) was deconvoluted into three peaks associated with Cu–N, C–N, and C=N at 401.1, 400.1, and 398.9 eV, respectively. Similarly, two distinct peaks appeared at 531.1 eV (Cu–O) and 532.5 eV (C–O). These results confirmed the coordination of Cu^{2+} to the imine and phenolic oxygen of the salphen core of pTPE-salphen. Interestingly, upon exposure of Cu^{2+}@pTPE-salphen to cysteine, the Cu 2p peaks in Cys–Cu@pTPE-salphen shifted to lower binding energies of 932.84 (Cu $2p_{3/2}$) and 952.59 eV (Cu $2p_{1/2}$), respectively. This suggests a significant change in the electronic environment of the copper metal ion. Moreover, Cys–Cu^{2+}@pTPE-salphen showed S 2p peaks at (Fig. 5c) 162.45 eV (Cu–S) and two additional peaks at 163.7 eV and 164.9 eV, corresponding to S $2p_{3/2}$ and S $2p_{1/2}$, confirming the coordination of Cys through thiolate. Notably, deconvolution of the O 1s spectrum of Cys–Cu^{2+}@pTPE-salphen resulted in multiple peaks corresponding to the COO^- group (532.8 eV) of cysteine and shifted Cu–O peak (530.6 eV) and free hydroxy groups (533.5 eV) potentially from the surface adsorbed moisture (Fig. 5d). Additionally, significant shifts were also observed in the N 1s spectrum. These results confirmed the successful coordination of cysteine to the Cu^{2+} of Cu^{2+}@pTPE-salphen. Such selective coordination of Cys and the presence of a high density of Cu^{2+} centers of Cu^{2+}@pTPE-salphen can further allow selective capture of cysteine. To demonstrate this, ^{1}H-NMR experiments were carried out by stirring a heterogeneous mixture of cysteine (8.25 mM in DMSO-d_6) and Cu^{2+}@pTPE-salphen (0–2.5 mg). The peaks corresponding to the CH of Cys at 4.2 ppm were monitored after the addition of Cu^{2+}@pTPE-salphen. As shown in Fig. 6 and S14, the peaks at 4.2 ppm gradually disappeared due to the adsorption of Cys within the porous network of Cu^{2+}@pTPE-salphen, due to its selective binding with Cu^{2+} present on the pore surface of the CMP network. Such capture of cysteine indicates the rapid diffusion kinetics of Cys, and the adsorption process enabled by the high surface area and porosity of Cu^{2+}@pTPE-salphen. To further confirm the capture of cysteine by the Cu^{2+}@pTPE-salphen CMP, EDS mapping analysis was performed before and after cysteine capture. As shown in Fig. S15–S20, Cu^{2+}@pTPE-salphen showed an appreciable distribution of 'Cu' throughout the polymer matrix while the Cys–Cu^{2+}@pTPE-salphen showed a uniform distribution of both 'Cu' and 'S' along with other elements (C, N, and O). These results indicate the efficiency of pTPE-salphen in the simultaneous detection of Cu^{2+} and tandem capture of cysteine. Unlike the previous reports where displacement of Cu^{2+} was observed from the COF matrix upon exposure to cysteine, pTPE-salphen resulted in the formation of distinct CMPs, *viz* Cu^{2+}@pTPE-salphen and Cys–Cu^{2+}@pTPE-salphen, as evidenced by their distinct

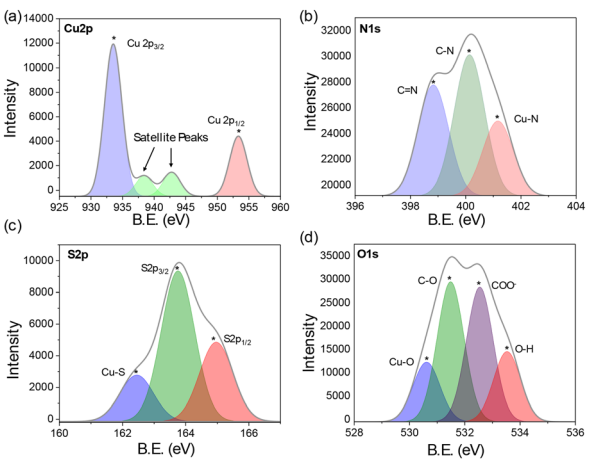

Fig. 5 Deconvoluted XPS spectra of (a) Cu 2p and (b) N 1s of Cu^{2+}@pTPE-salphen and (c) S 2p and (d) O 1s of Cys–Cu^{2+}@pTPE-salphen.

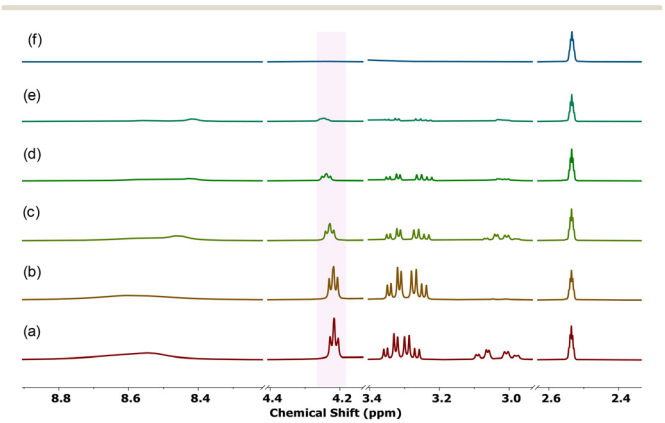

Fig. 6 ^{1}H NMR spectra of cysteine (8.25 mM in DMSO-d_6) (a) before and (b–f) after the addition of pTPE-salphen. The disappearance of cysteine peaks is due to the formation of Cys–Cu^{2+}@pTPE-salphen. Dibromoethane was used as an internal reference.

electronic properties supported by cyclic voltammetry, band gap analysis, and EIS measurements (Fig. S21–24).

3.6 Colorimetric test strips and RGB analysis

To further demonstrate the practical applicability of the pTPE-salphen sensor, paper-based test strips were fabricated and the colorimetric changes were captured at different stages. The test strips coated with pTPE-salphen showed a yellow color under day light, which turned into black upon exposure to 50 μM of Cu^{2+} solution due to the formation of the Cu^{2+}@pTPE-salphen CMP. Such dark coloration upon Cu^{2+} binding to the salen derivatives was previously reported and ascribed to the Cu^{2+}–salen complexation.[46–48] Subsequent exposure of Cu^{2+}@pTPE-salphen to the aqueous cysteine solution (0.5 mM) resulted in red coloration due to the formation of Cys–Cu^{2+}@pTPE-salphen. RGB analysis was performed on each of these strips to better visualize the colorimetric changes. As seen in Fig. 4b, the R/B value of pTPE-salphen dropped from 1.9 to 0.53 upon exposure to Cu^{2+} and increased to 1.8 upon exposure to cysteine, suggesting the successive interaction of Cu^{2+} and cysteine. Interestingly, the process is reversible, and the pTPE-salphen coated paper strips can be recovered by treating the Cu^{2+}@pTPE-salphen and Cys–Cu^{2+}@pTPE-salphen coated strips with EDTA and 1 N NaOH solutions, respectively, and the entire cycle (yellow ⇄ black ⇄ red) can be monitored through smartphone-assisted RGB analysis. So, the above results suggest that pTPE-salphen can act as both a colorimetric and fluorescent sensor for the selective detection of Cu^{2+} and the simultaneous capture of cysteine with remarkable recyclability properties. Such porous polymer sensors for reversible detection of Cu^{2+} and tandem capture of cysteine are rarely reported in the literature and represent a unique class of chemical sensors. Furthermore, the pTPE-salphen was easily transferred into a paper-strip sensor, demonstrating its potential for practical applications.

3.7 Recyclability studies

The recyclability of pTPE-salphen for chemical sensing in the dispersion phase was investigated at different stages. As shown in Fig. S25, the fluorescence of the pTPE-salphen was recovered upon treating the Cu^{2+}@pTPE-salphen (quenched state) with ethylene diamine tetraacetic acid (EDTA). The recovered fluorescent pTPE-salphen was used for further sensing cycles. At each cycle, pTPE-salphen showed excellent sensing response to Cu^{2+} and after 3 cycles, only a slight loss in the emission of the pTPE-salphen was observed, indicating the high recyclability of the CMP for Cu^{2+} sensing by the fluorometric method. The recovery of the CMP's fluorescence can be ascribed to the preferential binding of Cu^{2+} with EDTA over the salphen unit of pTPE-salphen, resulting in the removal of Cu^{2+} from the CMP matrix.

4. Conclusion

In conclusion, a new salphen-based conjugated microporous polymer (pTPE-salphen) integrating AIE-active fluorescent tetraphenylethene (TPE) and a metal ion-binding salphen core was synthesized and its dual-mode selective detection of Cu^{2+} and tandem capture of cysteine (Cys) were demonstrated. pTPE-salphen exhibited both fluorometric and colorimetric responses, *i.e.*, dual-mode response to Cu^{2+} in aqueous media. The Cu^{2+} complexation with the salphen unit of pTPE-salphen was responsible for fluorescence quenching, as evidenced by excited state lifetimes and a high K_{SV} constant value (K_{SV} = 8.12 × 10^6 M^{-1}). pTPE-salphen fluorometrically detected the Cu^{2+} up to 5.69 nM in the dispersion state and exhibited fluorescence response up to 10^{-11} M in paper strip contact mode, indicating its high applicability in sensing Cu^{2+} in real samples. Interestingly, Cu^{2+}@pTPE-salphen exhibited selective colorimetric changes upon exposure to cysteine due to Cu^{2+} and cysteine interactions and the tandem detection properties of pTPE-salphen were demonstrated. Unlike previously reported fluorescence turn-off/turn-on systems, pTPE-salphen enabled sequential dual-analyte sensing on a single platform without metal ion displacement, highlighting a new sensing mechanism in porous organic polymers. The entire sequential detection process of Cu^{2+} and cysteine using the pTPE-salphen sensor was visualized using smartphone-assisted RGB analysis, highlighting its possible practical applications. The tandem detection process was highly reversible, and the sensor was reusable over several cycles. Overall, this work elucidates a rational design approach for developing CMP-based chemical sensors that can show dual-mode chemical response and tandem detection properties, which are rare yet unique in the context of next-generation chemical sensors offering high selectivity and sensitivity in complex aqueous media. Future efforts will be focused on extending this design strategy to incorporate redox-active or orthogonal recognition units to enable multiplexed detection of biologically or environmentally relevant analytes, paving the way for advanced smart sensing materials.

Author contributions

NS and AK contributed equally to this work. VSM conceptualized, acquired funding, developed methodology, supervised the project, and wrote the manuscript. NS and AK contributed to carrying out experiments, formal analysis, data curation, investigation, methodology, and writing the initial draft. MY and SKR contributed to selected fluorescence experiments.

Conflicts of interest

There are no conflicts to declare.

Data availability

Supplementary information is available: The SI file contains additional experimental details, spectroscopic data (FTIR, NMR, UV–Vis, fluorescence), microscopic characterization data (XPS, SEM-EDS), titration details, cyclic voltammetry, impedance spectroscopy analysis, and supporting figures and tables relevant to the study. See DOI: **https://doi.org/10.1039/D5SD00097A**.

All the data supporting the conclusions of the work have been included in the main text. Additional data supporting this article have been included as part of the SI.

Acknowledgements

NS and AK contributed equally. AK thanks IIT Kanpur for the institute postdoc fellowship. NS, MY, SKR thank IIT Kanpur for the PhD research fellowship. VSM thanks the funding agencies IITK (Grant No. IITK/CHM/2022233), and Anusandhan National Research Foundation (ANRF), India (Grant No. SRG/2023/000062). The authors thank IITK for its infrastructure and analytical facilities.

References

1 A. Afrin, A. Jayaraj, M. S. Gayathri and C. A. P. Swamy, *Sens. Diagn.*, 2023, **2**, 988–1076.
2 W. P. Lustig, S. Mukherjee, N. D. Rudd, A. V Desai, J. Li and S. K. Ghosh, *Chem. Soc. Rev.*, 2017, **46**, 3242–3285.
3 A. Krężel and W. Maret, *Chem. Rev.*, 2021, **121**, 14594–14648.
4 Y. S. Kim, G. J. Park, S. A. Lee and C. Kim, *RSC Adv.*, 2015, **5**, 31179–31188.
5 S. Lee, G. Barin, C. M. Ackerman, A. Muchenditsi, J. Xu, J. A. Reimer, S. Lutsenko, J. R. Long and C. J. Chang, *J. Am. Chem. Soc.*, 2016, **138**, 7603–7609.
6 T. Chopra, S. Sasan, L. Devi, R. Parkesh and K. K. Kapoor, *Coord. Chem. Rev.*, 2022, **470**, 214704.
7 A. S. Murugan, A. Jegan, M. Pannipara, A. G. Al-Sehemi, S. M. Phang, G. G. Kumar and J. Annaraj, *Sens. Actuators, B*, 2020, **316**, 128082.
8 Y. Ding, R. Zhang, X. Qian, Y. Zhang, Y. Wei, L. Jin, Q. Wang and X. Cao, *New J. Chem.*, 2025, **49**, 6323–6331.
9 B. Mohan, N. M. Kunhumon and S. Shanmugaraju, *Sens. Diagn.*, 2023, **2**, 1158–1175.
10 C. E. Paulsen and K. S. Carroll, *Chem. Rev.*, 2013, **113**, 4633–4679.
11 A. Varghese, I. Gusarov, B. Gamallo-Lana, D. Dolgonos, Y. Mankan, I. Shamovsky, M. Phan, R. Jones, M. Gomez-Jenkins, E. White, R. Wang, D. R. Jones, T. Papagiannakopoulos, M. E. Pacold, A. C. Mar, D. R. Littman and E. Nudler, *Nature*, 2025, **643**, 776–784.
12 S. Wang, H. Li, H. Huang, X. Cao, X. Chen and D. Cao, *Chem. Soc. Rev.*, 2022, **51**, 2031–2080.
13 A. Dutta, A. Singh, X. Wang, A. Kumar and J. Liu, *CrystEngComm*, 2020, **22**, 7736–7781.
14 H. Shinziya, A. K. Das, M. S. Kumar, A. Nag and M. Dolai, *Sens. Diagn.*, 2025, **4**, 622.
15 S. Kumar Rajput, A. Kapoor, A. Yogi, V. Yarlagadda and V. S. Mothika, *Chem. – Asian J.*, 2024, **19**, e202400939.
16 M. Z. Alam, S. Ahmad, M. Mohasin, U. Salma, Alimuddin, H. Parveen, S. Mukhtar and S. A. Khan, *J. Fluoresc.*, 2025, DOI: **10.1007/s10895-025-04327-6**.
17 U. Salma, M. Z. Alam, S. Ahmad, M. Mohasin and S. A. Khan, *Inorg. Chim. Acta*, 2025, **582**, 122600.
18 W. He and Z. Liu, *RSC Adv.*, 2016, **6**, 59073–59080.
19 K. F. Kayani and A. M. Abdullah, *J. Food Compos. Anal.*, 2024, **135**, 106577.
20 K. F. Kayani and K. M. Omer, *New J. Chem.*, 2022, **46**, 8152–8161.
21 K. F. Kayani and C. N. Abdullah, *J. Fluoresc.*, 2025, **35**, 1125–1137.
22 L. Liu, H. Duan, H. Wang, J. Miao, Z. Wu, C. Li and Y. Lu, *ACS Omega*, 2022, **7**, 34249–34257.
23 L. R. Ahmed, A. F. M. EL-Mahdy, C.-T. Pan and S.-W. Kuo, *Mater. Adv.*, 2021, **2**, 4617–4629.
24 G. R. You, J. J. Lee, Y. W. Choi, S. Y. Lee and C. Kim, *Tetrahedron*, 2016, **72**, 875–881.
25 K. S. Park, M. Il Kim, M.-A. Woo and H. G. Park, *Biosens. Bioelectron.*, 2013, **45**, 65–69.
26 F. Yan, D. Shi, T. Zheng, K. Yun, X. Zhou and L. Chen, *Sens. Actuators, B*, 2016, **224**, 926–935.
27 J. Shen, X. Wen and Z. Fan, *Sens. Actuators, B*, 2023, **381**, 133436.
28 X.-L. Yang, C. Ding, R.-F. Guan, W.-H. Zhang, Y. Feng and M.-H. Xie, *J. Hazard. Mater.*, 2021, **403**, 123698.
29 S. K. Rajput and V. S. Mothika, *Macromol. Rapid Commun.*, 2024, **45**, 2300730.
30 Y. Li, S. Bi, F. Liu, S. Wu, J. Hu, L. Wang, H. Liu and Y. Hu, *J. Mater. Chem. C*, 2015, **3**, 6876–6881.
31 A. Kapoor, N. Sahoo, S. K. Rajput, P. K. Samanta and V. S. Mothika, *ACS Appl. Polym. Mater.*, 2025, **7**, 7672–7685.
32 A. Hazra and S. K. Samanta, *ACS Appl. Mater. Interfaces*, 2025, **17**, 21281–21294.
33 J. Chen, W. Yan, E. J. Townsend, J. Feng, L. Pan, V. d. A. Hernandez and C. F. J. Faul, *Angew. Chem., Int. Ed.*, 2019, **58**, 11715–11719.
34 V. S. Mothika, A. Räupke, K. O. Brinkmann, T. Riedl, G. Brunklaus and U. Scherf, *ACS Appl. Nano Mater.*, 2018, **1**, 6483–6492.
35 S. Sau, F. Banerjee and S. K. Samanta, *ACS Appl. Nano Mater.*, 2023, **6**, 11679–11688.
36 M. Donnier-Maréchal, S. Abdullayev, M. Bauduin, Y. Pascal, M.-Q. Fu, X.-P. He, E. Gillon, A. Imberty, E. Kipnis, R. Dessein and S. Vidal, *Org. Biomol. Chem.*, 2018, **16**, 8804–8809.
37 J.-B. Xiong, H.-T. Feng, J.-P. Sun, W.-Z. Xie, D. Yang, M. Liu and Y.-S. Zheng, *J. Am. Chem. Soc.*, 2016, **138**, 11469–11472.
38 H. Qu, X. Tang, X. Wang, Z. Li, Z. Huang, H. Zhang, Z. Tian and X. Cao, *Chem. Sci.*, 2018, **9**, 8814–8818.
39 P. Ju, W. Qi, B. Guo, W. Liu, Q. Wu and Q. Su, *Catal. Lett.*, 2023, **153**, 2125–2136.
40 M. S. Woolf, L. M. Dignan, A. T. Scott and J. P. Landers, *Nat. Protoc.*, 2021, **16**, 218–238.

41 B. Khanal, P. Pokhrel, B. Khanal and B. Giri, *ACS Omega*, 2021, **6**, 33837–33845.
42 L. Yu, L. Bai, J. Liu, J. Yang, S. Meng, T. Yang, Y.-H. Yang and R. Hu, *Talanta*, 2025, **295**, 128346.
43 Y. Hui, H. Guo, M. Wang, L. Peng, B. Ren, Y. Ma and W. Yang, *Talanta*, 2025, **292**, 127990.
44 Z. Zhou, X. Wen, C. Shi, L. Wu, Z. Long, J. He and X. Hou, *Food Chem.*, 2023, **417**, 135883.
45 G. Singh, D. Bains, H. Singh, N. Kaur and N. Singh, *ACS Appl. Nano Mater.*, 2019, **2**, 5841–5849.
46 D. Mohapatra, S. A. Patra, P. Das Pattanayak, G. Sahu, T. Sasamori and R. Dinda, *J. Inorg. Biochem.*, 2024, **253**, 112497.
47 P. Ju, Q. Su, Z. Liu, X. Li, B. Guo, W. Liu, G. Li and Q. Wu, *J. Mater. Sci.*, 2019, **54**, 851–861.
48 H.-T. Feng, S. Song, Y.-C. Chen, C.-H. Shen and Y.-S. Zheng, *J. Mater. Chem. C*, 2014, **2**, 2353–2359.